8-15-2023

Mechanical stiffness and anisotropy measured by MRE during brain development in the minipig

Shuaihu Wang
Washington University in St. Louis
Charlotte A Guertler
Washington University in St. Louis
Ruth J Okamoto
Washington University in St. Louis
Curtis L Johnson
University of Delaware
Matthew D J McGarry
Dartmouth College

See next page for additional authors

NeuroImage 277 (2023) 120234

Contents lists available at ScienceDirect

NeuroImage

journal homepage: www.elsevier.com/locate/neuroimage

Mechanical stiffness and anisotropy measured by MRE during brain development in the minipig

Shuaihu Wang[a], Charlotte A. Guertler[a], Ruth J. Okamoto[a], Curtis L. Johnson[b], Matthew D.J. McGarry[c], Philip V. Bayly[a,d,*]

[a] Mechanical Engineering and Material Science, Washington University in St. Louis, United States
[b] Biomedical Engineering, University of Delaware, United States
[c] Thayer School of Engineering, Dartmouth College, United States
[d] Biomedical Engineering, Washington University in St. Louis, United States

ARTICLE INFO

Keywords:
Magnetic resonance elastography
Diffusion tensor imaging
Stiffness
Anisotropy
Brain development

ABSTRACT

The relationship between brain development and mechanical properties of brain tissue is important, but remains incompletely understood, in part due to the challenges in measuring these properties longitudinally over time. In addition, white matter, which is composed of aligned, myelinated, axonal fibers, may be mechanically anisotropic. Here we use data from magnetic resonance elastography (MRE) and diffusion tensor imaging (DTI) to estimate anisotropic mechanical properties in six female Yucatan minipigs at ages from 3 to 6 months. Fiber direction was estimated from the principal axis of the diffusion tensor in each voxel. Harmonic shear waves in the brain were excited by three different configurations of a jaw actuator and measured using a motion-sensitive MR imaging sequence. Anisotropic mechanical properties are estimated from displacement field and fiber direction data with a finite element- based, transversely-isotropic nonlinear inversion (TI-NLI) algorithm. TI-NLI finds spatially resolved TI material properties that minimize the error between measured and simulated displacement fields. Maps of anisotropic mechanical properties in the minipig brain were generated for each animal at all four ages. These maps show that white matter is more dissipative and anisotropic than gray matter, and reveal significant effects of brain development on brain stiffness and structural anisotropy. Changes in brain mechanical properties may be a fundamental biophysical signature of brain development.

1. Introduction

Adolescence is a critical period for human brain development that is accompanied by structural changes in the brain that may significantly impact its function. For instance, the fronto-cortical and fronto-striatal circuits change until early adulthood, associated with the development of higher cognitive skills (Barnea-Goraly et al., 2005). Adolescence is also an important period for the development of neuropsychiatric disorders (McGorry et al., 2011). Brain structural abnormalities are observed in major depressive disorder, bipolar disorder, and schizophrenia (Opel et al., 2020). These changes in structure affect the mechanical properties of brain tissue (Sack et al., 2013). Thus, characterization of mechanical properties during brain development is important for understanding of normal brain structure, function, and health.

Magnetic resonance elastography (MRE) is an emerging imaging technique for probing brain mechanical properties; which in turn depend on tissue microstructure (Manduca et al., 2001; Mariappan et al., 2010). In MRE mechanical wave propagation is measured with a modified magnetic resonance imaging (MRI) pulse sequence that includes harmonic, motion-sensitizing gradients to measure the dynamic displacement field. The displacement field is then "inverted" to estimate mechanical properties, such as stiffness and damping (Zhang et al. 2011; Johnson et al., 2013), usually assuming an underlying viscoelastic material model. The mechanical properties of tissue can be calculated using local frequency estimation (Manduca et al., 1996), direct inversion of the viscoelastic shear wave equation (Oliphant et al., 2001; Sinkus et al., 2005; Okamoto et al., 2011), or finite element (FE) methods (Van Houten et al., 2002; McGarry et al., 2012; Fovargue et al., 2018).

Previous work has established the utility of MRE for mechanical characterization of tissues like brain, liver, and muscle (Klatt et al. 2007; Sack et al., 2009a). MRE has been used to study changes in stiffness and viscosity due to aging (Sack et al., 2009b; Hiscox et al., 2021), disease (Hiscox et al., 2020) and injury (Boulet et al. 2013). How-

* Corresponding author at: Mechanical Engineering and Material Science, Washington University in St. Louis, Jubel Hall, 1 Brookings Drive, St., Louis, MO 63130, United States.
E-mail address: pvb@wustl.edu (P.V. Bayly).

https://doi.org/10.1016/j.neuroimage.2023.120234.
Received 15 February 2023; Received in revised form 12 May 2023; Accepted 15 June 2023
Available online 25 June 2023.

ever, most MRE studies use inversion models with the simplifying assumption of mechanical isotropy, which in anisotropic tissue will lead to uncertainty and increased variability in mechanical property estimates (Anderson et al., 2016). Several anisotropic MRE methods have been proposed, which vary in the underlying material model and the number of parameters to be estimated. For example, a nine-parameter model was developed by Romano and collaborators to characterize white matter (WM) tracts (Romano et al., 2012; Romano et al., 2014). Others have proposed models with smaller numbers of free parameters. A two-parameter model has been used to characterize breast tissue (Sinkus et al., 2005) and skeletal muscle (Green et al., 2013). An incompressible, transversely isotropic material model with three parameters (Feng et al., 2013; Tweten et al., 2015; Schmidt et al. 2016; Guo et al., 2015; Guidetti M and Royston TJ., 2018) has previously been used to characterize anisotropic phantom (Guidetti M et al., 2021) and fibrous tissues, including brain WM (Schmidt et al., 2018; Smith et al., 2020) and muscle (Guertler et al., 2020; Hou et al., 2022). Miller et al. (2018) used both 3- and 5-parameter transversely isotropic material models to describe cardiac muscle. Although these anisotropic MRE methods vary in terms of model complexity, they share a common requirement for sufficient displacement data to estimate the material parameters. Tweten et al. has demonstrated that multiple shear waves, both slow (pure-shear) and fast (quasi-shear), with different propagation directions, must be present in the displacement field for accurate parameter estimates from local frequency estimation of directionally filtered waves (Tweten et al., 2018). Multi-excitation MRE uses more than one actuator or actuator location to provide distinct displacement fields (Anderson et al., 2016), and has emerged as a promising technique for providing sufficiently diverse shear wave data for anisotropic inversion (Smith et al. 2020).

The choice of inversion method is an important factor in estimation of mechanical parameters by MRE. The finite-element-based nonlinear inversion (NLI) is an iterative FEM inversion technique that accounts for local inhomogeneity and wave reflection effects up to the limit of the displacement resolution (Van Houten et al., 2002). McGarry et al. (2012) developed a multi-resolution finite element approach for NLI, allowing independent discretization of the displacements and each mechanical parameter. The three-parameter transversely isotropic (TI) model has been incorporated into the NLI framework to create an estimation scheme, which we denote TI-NLI, designed to recover heterogeneous, anisotropic properties. TI-NLI has been shown to recover accurate (within 1.3% of true values) heterogenous parameter fields using synthetic data in the presence of measurement noise, and repeatable (coefficient of variation < 7.7% over 10 scans) property estimates for *in vivo* human brain (McGarry et al., 2022).

Diffusion tensor imaging (DTI), a magnetic resonance modality which detects water diffusion in biological tissues at a microstructural level (Basser et al., 1996), is a powerful technique to explore brain tissue organization and maturation (Faria et al., 2010). WM maturation, especially the process of myelination, appears to be reflected by an increase of diffusion anisotropy; this can be utilized to characterize different stages of early brain development (Qiu et al., 2015). Some recent studies have used DTI to incorporate fiber orientation of brain tissue into computational models to investigate the effect of axonal fibers on the mechanical behavior of brain tissue (Garimella et al., 2017; Giordano et al., 2017; McGarry et al., 2021).

The minipig is commonly utilized in brain research, including investigation of brain mechanical properties (Guertler et al., 2018) and mechanisms of traumatic brain injury (Atlan et al., 2018; Atlan et al., 2019; Netzley et al., 2021) due to its anatomical and physiological similarities to humans (Schomberg et al., 2016). The minipig has a gyrencephalic brain with a ratio of cerebral WM to gray matter (GM) which is similar to humans (Swindle et al. 2012), and on the order of 1 to 3. Fil et al (2021) reported a GM/WM ratio of approximately 2.2 in the porcine brain. Further, while brain development in the minipig occurs over a compressed time period relative to humans, myelination and brain WM development are analogous in juvenile minipigs and adolescent humans. Scant myelination was observed in the 2-month-old minipig but increased by 6 months of age when the pig is sexually mature (Fang et al., 2005). Therefore, longitudinal studies in the minipig are logical and feasible for investigating changes in the brain during development.

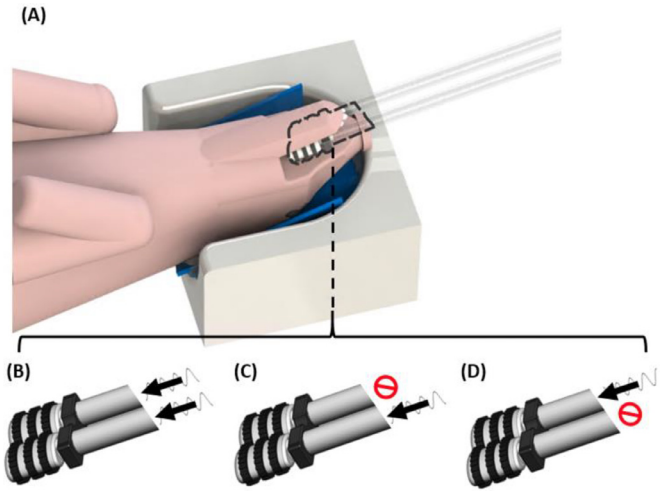

Fig. 1. (A) Experimental set-up for MRE. Anesthetized minipig is placed in dorsal recumbency with its head placed in the lower part of the Seimens Head/Neck20 coil. Insets show the custom actuator, which is inserted to the mouth, preloaded against the molars, and driven by the Resoundant™ pneumatic driver. Three configurations are used to induce shear waves in brain at 100 Hz. (B) "Both" actuator configuration. (C) "Right" actuator configuration. (D) "Left" actuator configuration.

The primary objective of this paper is thus to measure anisotropic mechanical properties in the minipig brain during brain development, and characterize changes that may occur over this period. To this end, shear wave displacement fields were obtained by multiple MRE acquisitions using three different mechanical actuator configurations in juvenile Yucatan minipigs aged from 3 to 6 months. Structural anisotropy (fiber orientation) was characterized by the diffusion tensors estimated by DTI. Anisotropic mechanical parameters were then estimated from the combined MRE and DTI data via the NLI algorithm. Finally, longitudinal changes in brain tissue properties were evaluated over this period of brain development.

2. Methods

2.1. Experimental methods and data acquisition

Six juvenile female Yucatan minipigs (Fig. S1) were scanned (Siemens Prisma® 3T scanner). Each animal was scanned once per month for a total of four scans per animal. Ages at initial scan were 2.7-3.0 months (weights 9.7-12.6 kg) and at final scan were 5.7-6.1 months (weights 22.4-31.5 kg). All studies were approved by the Washington University in St. Louis Institutional Animal Care and Use Committee and supervised by veterinary staff. Animals were sedated with Telazol-Ketamine-Xylazine (TKX) intramuscular injection. An IV catheter and endotracheal tube were placed prior to scanning, and anesthesia was maintained continuously with 1-2% isoflurane during scanning via endotracheal tube. Temperature, pulse, respiration, and SPO2 were monitored by veterinary staff during the scan. The anesthetized minipigs were positioned in dorsal recumbency on the scanner table with head placed in the bottom half of the Siemens Head/Neck 20 coil. Bean bags and foam padding were used to maintain a stable head position (Fig. 1A).

Skull vibrations and shear waves in the brain were induced at a frequency of 100 Hz using a custom multi-directional jaw actuator (Guertler et al., 2018). Harmonic pressure was generated by an active pneumatic driver (Resoundant™, Rochester, MN) and transmitted by plastic tubing to the passive jaw actuator, which consists of two small, flexible plastic bottles. After positioning the minipig, the custom actuator was inserted into the animal's mouth, with the bottles pre-loaded against the rear molars to minimize slippage between the teeth and actuator. MRE was performed using three actuator configurations to produce different motions in brain. The three actuator configurations were: (1) both actuator bottles actuated in phase ("Both" actuation, Fig. 1B); (2) only the left side actuated ("Left" actuation, Fig. 1C); (3) only the right side actuated ("Right" actuation, Fig. 1D).

MRE phase-contrast images of the harmonic displacement field were acquired with 1.5 mm isotropic resolution covering a volume of 180×180×72 mm^3 (120×120 matrix, 48 slices) using a 2D multishot spiral sequence (Johnson et al., 2013) with OSCILLATE ("Observing Spatiotemporal Correlations for Imaging with Low-rank Leveraged Acceleration in Turbo Elastography") acceleration (McIlvain et al., 2022). Multiple sinusoidal motion-encoding cycles of gradient strength 70 mT/m were synchronized with motion to induce phase contrast proportional to displacement (1.498 microns/rad) and collect 8 temporal samples acquired per period of harmonic motion. The repetition time (TR) was 4800 ms and the echo time (TE) was 60 ms. Images were spatially phase-unwrapped using open-source software (FSL Prelude) (Smith et al., 2004).

T1-weighted and T2-weighted anatomical MR images were acquired during each scan. The image volumes were acquired at 0.8 mm isotropic resolution with a matrix size of 256×256 and 192 slices for an image volume of 205 mm x 205 mm x 154 mm. Two averages were acquired for each image set to improve signal-to-noise ratio.

Diffusion tensor imaging (DTI) was performed to estimate WM fiber direction. Diffusion weighted images were acquired with the same 1.5 mm isotropic voxel resolution and center of slice groups as the MRE scan but in a larger imaging volume of 192×192×72 mm^3 (128×128 matrix, 48 slices) using a single-shot echo-planar imaging (EPI) acquisition. Diffusion images were obtained using 30 diffusion-weighted directions with two averages. Images were corrected for motion and eddy currents with TORTOISE v3.2 (Pierpaoli et al., 2010), then corrected for EPI distortion using DRBUDDI (Irfanoglu et al., 2015). Nonlinear tensor fitting was performed to estimate the diffusion tensor at each voxel. Fractional anisotropy (FA) was calculated from the diffusion tensor eigenvalues (λ_1, λ_2, and λ_3),

$$\mathrm{FA} = \sqrt{\frac{3}{2}}\frac{\sqrt{\left(\lambda_1-\hat{\lambda}\right)^2+\left(\lambda_2-\hat{\lambda}\right)^2+\left(\lambda_3-\hat{\lambda}\right)^2}}{\sqrt{\lambda_1^2+\lambda_2^2+\lambda_3^2}}, \tag{1}$$

where $\hat{\lambda} = (\lambda_1+\lambda_2+\lambda_3)/3$. Fiber direction was assumed to be the direction of the first principal eigenvector of the diffusion tensor (the direction of maximal diffusivity).

2.2. Data analysis

2.2.1. Bulk motion and dynamic deformation

Displacement field data were checked for sign and direction consistency (Supplementary Fig. S7), and fitted to a model of rigid-body displacement to estimate rigid-body motion ("bulk motion"). Dynamic deformation ("wave motion") was isolated by subtracting the rigid-body motion from the total displacement field (Badachhape et al., 2017).

2.2.2. Transversely Isotropic Nonlinear Inversion

TI-NLI was performed on MRE displacement fields to estimate the stiffness and anisotropy of the minipig brain using the nearly incompressible transversely isotropic (NITI) material model (McGarry et al., 2021). Three parameters describe the response of an NITI material during small deformations (Feng et al., 2013):

(1) $G^* = G' + iG''$, the complex shear modulus in the plane of isotropy;
(2) $\phi = G_1'/G' - 1$, the relative difference in shear storage modulus for shear in planes perpendicular to the plane of isotropy, G_1', relative to the in-plane shear modulus, G';
(3) $\zeta = E_1'/E' - 1$, the relative difference in Young's modulus for stretch along the fiber axis, E_1', relative to Young's modulus for stretch normal to the fiber axis, E'.

At the limit of incompressibility, the two tensile moduli are related to these three parameters by $E_1' = G'(4\zeta+3)$ and $E' = G'(4\zeta+3)/(\zeta+1)$ (Tweten et al., 2015). The complex shear modulus is reformulated to baseline shear stiffness $\mu = 2|G^*|^2/(G' + |G^*|)$ (Manduca et al., 2001), and damping ratio $\xi = G''/2G'$ (McGarry and Van Houten, 2008). The baseline shear stiffness governs the wave speed of harmonic shear waves in the plane of isotropy, while the damping ratio describes the attenuation of harmonic motion.

Subzone-based NLI is based on an iterative minimization of an objective function (Φ) for each subzone:

$$\Phi(\theta) = \sum_{i=1}^{N_m}\left\{\left(u_{m(i)} - u_{c(i)}(\theta)\right)\left(u_{m(i)} - u_{c(i)}(\theta)\right)^*\right\}, \tag{2}$$

where $u_{m(i)}$ denotes the complex-valued amplitude of the i th displacement measurement, $u_{c(i)}(\theta)$ are the analogous displacement calculated with the forward computational model based on the current estimate of the properties, θ, N_m is the number of subzones and $*$ represents the complex conjugate (Van Houten et al., 2001). In this work, 16 mm cubic subzones were used, which is near 0.75 shear waves per zone, as previously shown to produce stable estimates (parameter estimates are insensitive to variations in subzone size near this value) in NLI (Anderson et al., 2017).

TI-NLI can incorporate data (displacement fields) from multiple actuation scenarios. Four combinations of displacement fields, BLR, BL, BR and LR, were used as input to TI-NLI to estimate the material properties. The initials "B", "L" and "R" refer to displacement field obtained by using "Both", "Left, and "Right" actuator configurations, respectively (Fig. 1). "BLR" means the inversion uses data (wave fields) generated by all three actuator configurations; "BL", "BR", or "LR" mean that data from the two specified configurations were used. For each inversion, the algorithm uses all the data from the included configurations. In a subset of scans, TI-NLI and isotropic NLI were performed using only data from a single actuator configuration.

Images were masked prior to NLI by manually segmenting brain regions using ITK-Snap (Yushkevich et al., 2006) (Fig. 2A-B). The medulla, pons, and olfactory bulbs were then removed prior to the estimation of material parameters since the size of these regions are relatively small compared to both the wavelengths of shear waves and the subzone size. Voxels used for NLI ("brain volume of interest" or "brain VOI", Fig. 2C) comprise ~80% of total brain voxels for all scans. Voxels inside this region with both FA greater than 0.2 (Fil et al, 2021) and with diffusion consistent with a prolate or "linear" diffusion ellipsoid ($\lambda_1 - \lambda_2 > \lambda_2 - \lambda_3$) (Westin et al., 2002) are denoted as WM for data analysis (Fig. 2D), typically ~25% of the brain VOI. GM voxels were defined as voxels within the brain VOI with FA < 0.2 (approximately 55% of the brain VOI). Cerebrospinal fluid (CSF) was automatically segmented and removed from all analyzed regions (brain VOI, GM and WM) using a threshold that eliminates hyperintense voxels in T2W images interpolated onto MRE images. Voxels with FA>0.2 and oblate or "planar" diffusion ellipsoids, $(\lambda_1 - \lambda_2) < (\lambda_2 - \lambda_3)$, are not included in either WM or GM regions defined here.

2.2.3. Statistical analysis

For statistical analysis, mean values of FA and parameters estimated by TI-NLI (using the BLR combined data set) in each brain volume and WM and GM sub-volumes were treated as individual data points, with means and standard deviations computed over all scans. MRE data from animal MP1 at 3 months were dropped due to excessive phase wrap in

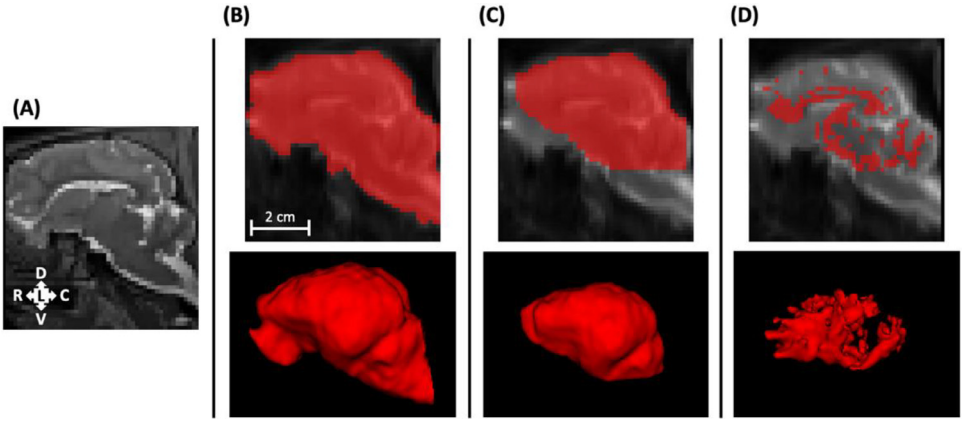

Fig. 2. (A) T2-weighted image slice in sagittal plane. (B) Brain mask used for MRE data processing in animal MP4 at 5 months. (C) Brain volume of interest ("brain VOI") without medulla, pons and olfactory bulbs used for NLI in animal MP4 at 5 months. (D) White matter sub-volume in animal MP4 at 5 months.

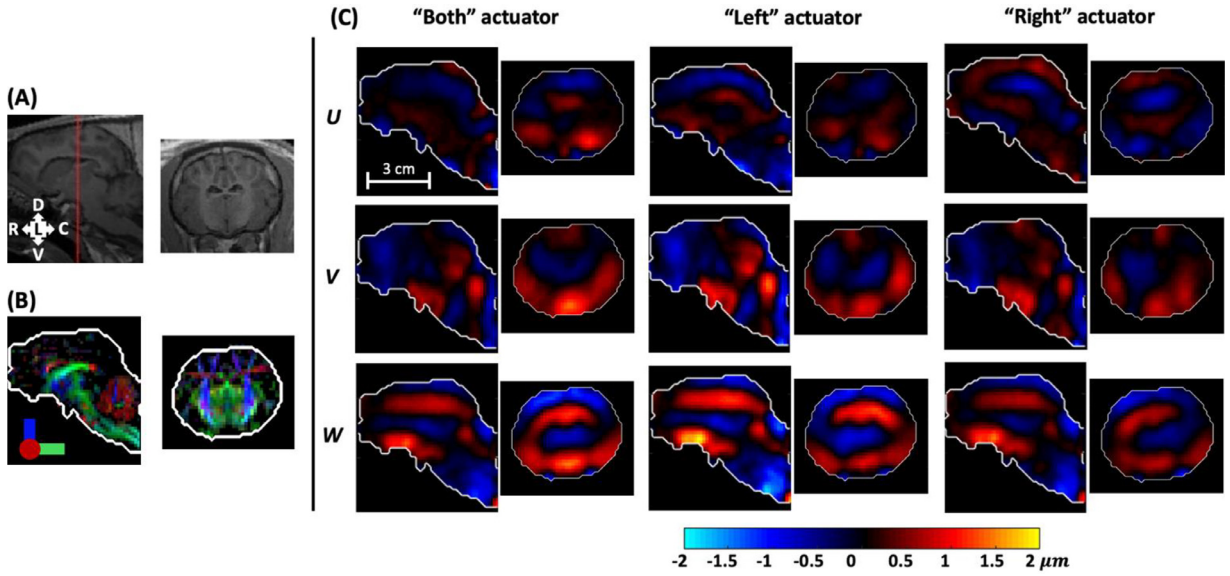

Fig. 3. Example anatomical, DTI, and MRE displacement images. (A) T1-weighted image slices in sagittal and axial planes. (B) Directionally encoded DTI color map where colors (red = RL, green= RC, blue= DV) indicate direction of maximum diffusivity and brightness indicates strength of anisotropy. (C) MRE data: U, V and W wave displacement components corresponding to RL, DV, RC motion, respectively. DTI: diffusion tensor imaging; DV: dorsal-ventral; RC: rostral-caudal; RL: right-left; MRE: magnetic resonance elastography.

the raw MRE (phase contrast) images. The four mechanical parameters were each fitted to a linear mixed-effects model (LMEM) with age and tissue type (WM/GM) as predictor variables and scan date as a repeated measure, using the "*fitlme*" function in the Matlab Statistics and Machine Learning Toolbox, v. R2022a (Mathworks, Natick MA). The LMEM equation for each estimated mechanical property was of the form:

$$y_n = b_i + m_i x + \in_k + \in_n \quad (3)$$

where y_n is the value of the mechanical property for the n^{th} scan date, x is the age of the animal (in months, relative to the initial scanning age), m_i and b_i are the slope and intercept for the ith tissue type ($i = 1, 2$), $\in_k$ is a random effect for each scan date, and $\in_n$ is the residual error after fitting. The fitting was followed by an F-test to determine significance for each fixed effect; $p < 0.05$ was considered statistically significant. FA from DTI was analyzed using similar method, but only with age as a predictor variable and each pig as a repeated measure.

3. Results

Fig. 3 shows examples of wave motion for one axial and one sagittal slice of a representative minipig brain. Displacement components were measured in all three directions: U denotes the component in the right-left (RL) direction; V the component in the dorsal-ventral (DV) direction and W the component in the rostral-caudal (RC) direction. The V component of wave motion is the dominant component excited by all three actuator configurations. The maximum displacement amplitude is about 2 μm.

Fig. 4 shows the mean FA values calculated from diffusion tensors of all six animals at different ages. The mean FA values increase slightly with age, and a significant effect of age on FA was observed in both the whole brain VOI ($p = 0.0022$) and the WM sub-volume ($p = 0.0009$).

Representative maps of shear stiffness, μ, damping ratio, ξ, shear anisotropy, ϕ, and tensile anisotropy, ζ, for three axial slices of a representative minipig brain estimated using TI-NLI with four different combinations of input fields for animal MP4 at 5 months are shown in Fig. 5. The TI-NLI-estimated fields of all four parameters are similar across the different input combinations. Fig. 6 displays fields of voxel-wise mean values and standard deviations of these four parameter estimates for the different input combinations. The mean parameter fields appear to most closely resemble the parameter values obtained using all actuator (BLR) data. The relatively low values of the standard deviations (on the order of 10% of the mean values) indicate low variability and thus good repeatability of the acquisition and estimation methods.

Fig. 7 displays representative TI-NLI-estimated material properties using the "BLR" input in both the whole brain VOI and the WM sub-

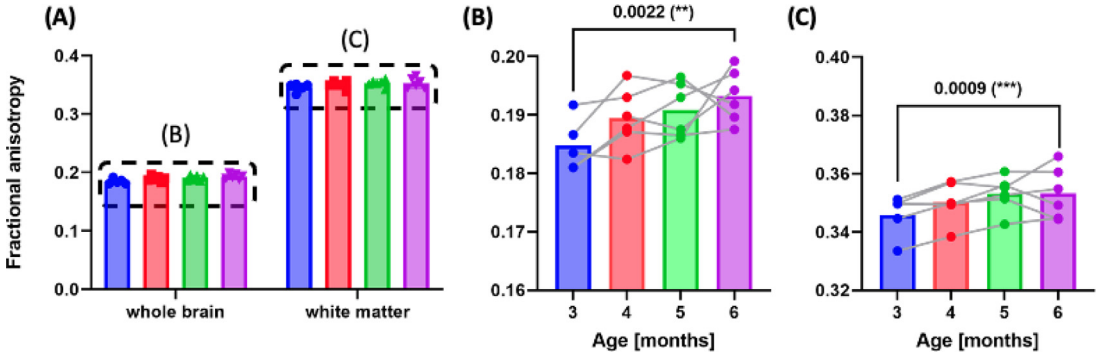

Fig. 4. (A) Mean fractional anisotropy (FA) for all six minipigs. Each marker represents the mean value for each individual minipig. (B) FA in the entire brain VOI (magnified scale). (C) FA in white matter (magnified scale). Lines connect data from each animal.

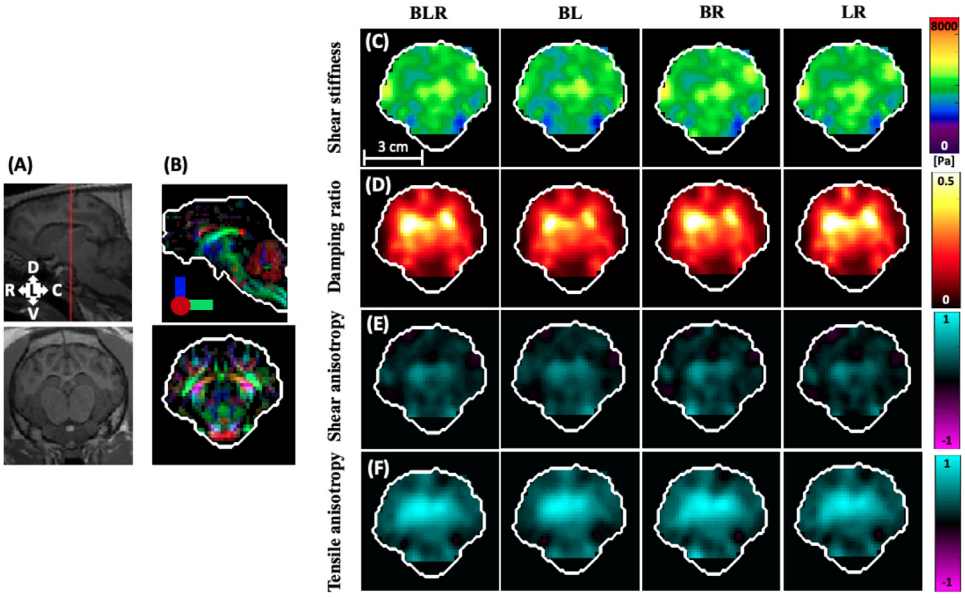

Fig. 5. Mechanical properties estimated by NLI using different combinations of input data sets (each set from a different actuator configuration) for three axial slices of minipig brain in animal MP4 at 5 months. B: "Both" actuator configuration; L: Left" actuator configuration; R: "Right" actuator configuration. (A) T1-weighted images in sagittal and axial planes with axial slice position shown in sagittal image. (B) Directionally encoded DTI color map (red = RL, green= RC, blue= DV). (C) Shear stiffness (μ). (D) Damping ratio (ξ). (E) Shear anisotropy (ϕ). (F) Tensile anisotropy (ζ).

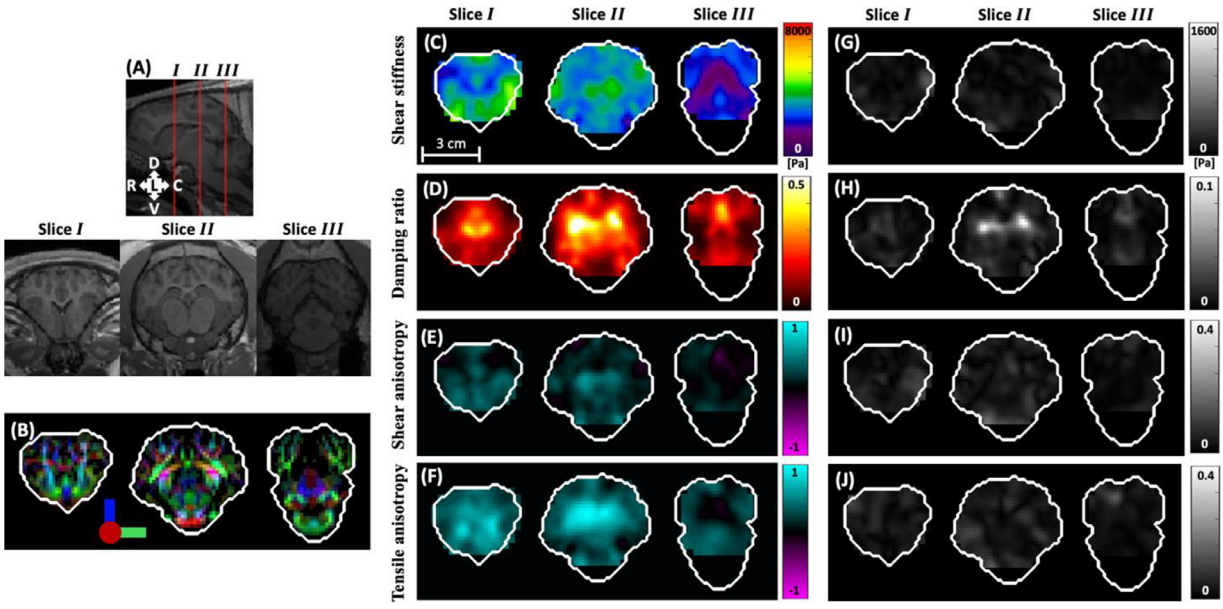

Fig. 6. Mechanical properties estimated by NLI using all combinations of input data sets (actuator configurations) for three axial slices of minipig brain in animal MP4 at 5 months. (A) T1-weighted images in sagittal and axial planes with axial slice positions shown in sagittal image. (B) Directionally encoded DTI color map (red = RL, green= RC, blue= DV). (C, G) Shear stiffness (μ). (D, H) Damping ratio (ξ). (E, I) Shear anisotropy (ϕ). (F, J) Tensile anisotropy (ζ). Panels (C-F) show for each voxel the mean value of property estimates from the BLR, BL, BR and LR cases. Panels (G-J) show for each voxel the standard deviation of property estimates for the four cases.

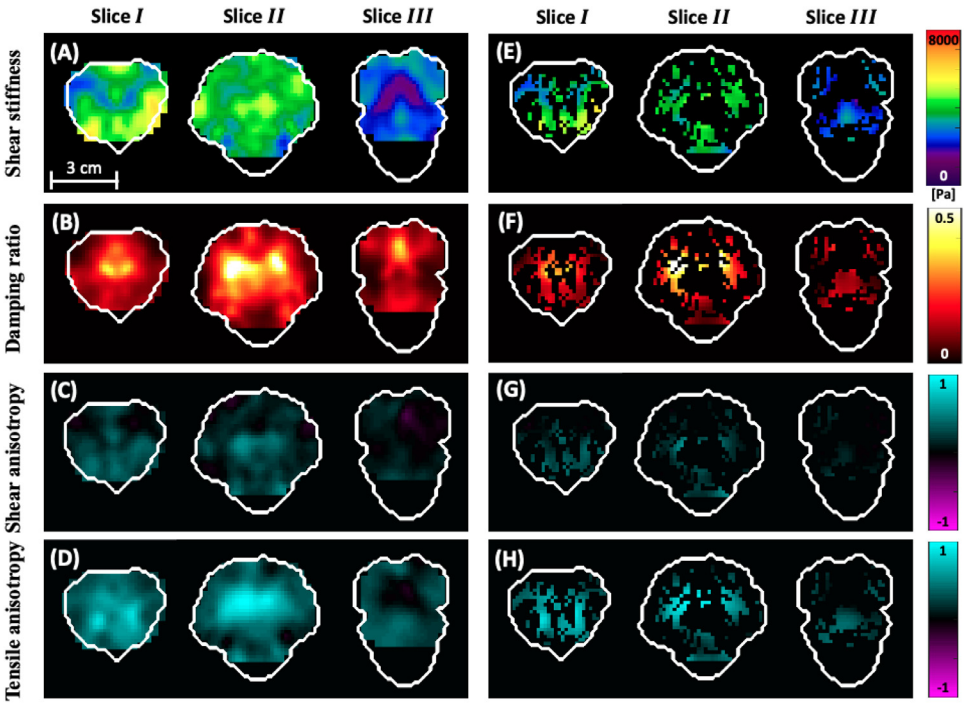

Fig. 7. Mechanical properties estimated by NLI using the combined BLR data set for three axial slices of minipig brain in animal MP4 at 5 months. The slice positions are same as in Fig. 6. (A, E) Shear stiffness (μ). (B, F) Damping ratio (ξ). (C, G) Shear anisotropy (ϕ). (D, H) Tensile anisotropy (ζ). Panels (A-D) show estimates throughout the entire brain. Panels (E-H) show estimates in white matter.

volume in animal MP4 at 5 months. Estimates of damping ratio, ξ, shear anisotropy, ϕ, and tensile anisotropy, ζ, appear noticeably higher in WM voxels. The mean values of these four parameters in the entire brain VOI, the WM sub-volume, and the GM sub-volume are depicted in Fig. 8. Some common features emerge in these six animals at 3-6 months. Mean values of damping ratio, ξ, shear anisotropy, ϕ, and tensile anisotropy, ζ, are markedly higher in WM, and a small but consistent difference in baseline shear stiffness is seen between WM and GM.

Estimated mechanical parameters in WM and GM are shown versus age in Fig. 9, along with key results of the linear mixed-effects models. Baseline shear stiffness was slightly higher in WM than GM and increased significantly with age in both regions ($p = 0.0029$ in WM and $p = 0.0562$ in GM). The damping ratio was higher in WM than GM, and did not change with age. Shear anisotropy was higher in WM than in GM, and did not depend on age ($p = 0.5472$ in WM and $p = 0.8048$ in GM). Finally, tensile anisotropy was greater in WM than GM. Tensile anisotropy appeared to decrease in both WM and GM, but the slope was not statistically significant in either ($p = 0.2072$ in WM and $p = 0.7238$ in GM). Overall, WM appears stiffer, more dissipative, and more anisotropic then GM, and tissue stiffness increases with age over this period. Numerical values of parameter estimates are tabulated in Supplementary Table ST3.

4. Discussion

This study provides the first estimates of anisotropic mechanical properties by MRE during brain development in a large animal model: the minipig. Since minipigs are sexually mature by six months of age, the compressed development period positions the minipig as a valuable research model for adolescent brain development. We observed a subtle increase in diffusion anisotropy (FA) with age, which is consistent with prior studies in minipigs (Ryan et al., 2018) and in adolescent human brain WM development (Ashtari et al., 2007). This is likely due to increased myelination of WM microstructures (Mädler et al., 2008).

A small, but statistically-significant increase in baseline shear stiffness, μ, with age was observed, but no significant effects of age were observed on damping ratio, ξ, shear anisotropy, ϕ, or tensile anisotropy, ζ. Comparing properties in WM and GM, shear stiffness, damping ratio, shear anisotropy and tensile anisotropy are all higher in WM than GM. A key point is that the higher stiffness of WM relative to GM is attributable to the anisotropic mechanical parameters. The baseline shear stiffness of WM describes only the resistance to shear in the plane normal to the fiber axis. However, WM behaves as an even stiffer material in all other deformations due to the anisotropy of WM. WM is stiffer in shear in any plane containing the fiber direction (due to positive shear anisotropy, ϕ), and WM is stiffer in tension in any direction with a component of fiber direction (due to positive tensile anisotropy, ζ).

To improve the accuracy and robustness of mechanical properties and anisotropy parameter estimates, MRE was performed using data from three configurations of an actuator that imparted different types of wave motion to the brain, providing four combinations of input data for the TI-NLI algorithm. The three actuator configurations, “Both”, “Left”, and “Right” lead to different motion patterns with some common features. The wave displacement fields are on the order of 1-2 microns, which are similar in magnitudes to human MRE studies performed with a “paddle actuator” (Clayton et al., 2012) and with a “pillow” actuator (Badachhape et al., 2017), as well as to those in a previous study in the mature minipig brain (Guertler et al., 2018).

The wave fields from the three actuator configurations provide four combinations of input to the TI-NLI inversion algorithm, and the estimated mechanical properties with these four combinations exhibit qualitatively and quantitatively similar patterns. Variations in estimates between different combinations were typically less than 100 Pa in shear stiffness, less than 0.02 for damping ratio, and less than 0.05 for shear anisotropy and tensile anisotropy parameters (Supplementary Fig. S3). This provides evidence that the multi-excitation, TI-NLI-based, anisotropic MRE approach is sufficiently stable to reproducibly estimate these anisotropic mechanical properties in the minipig brain. Relatively higher standard deviations were observed near boundaries for all four parameters. This suggests some sensitivity of TI-NLI to the boundary of the computational domain where the overlapping subzones cannot mitigate noise in the measured displacements applied as boundary conditions (McGarry et al., 2021). Shear waves also dissipate energy in the brain; the loss of amplitude causes the estimation of these material properties in the center of the brain to be more affected by noise, which apparently leads to relatively higher standard deviations of estimates in

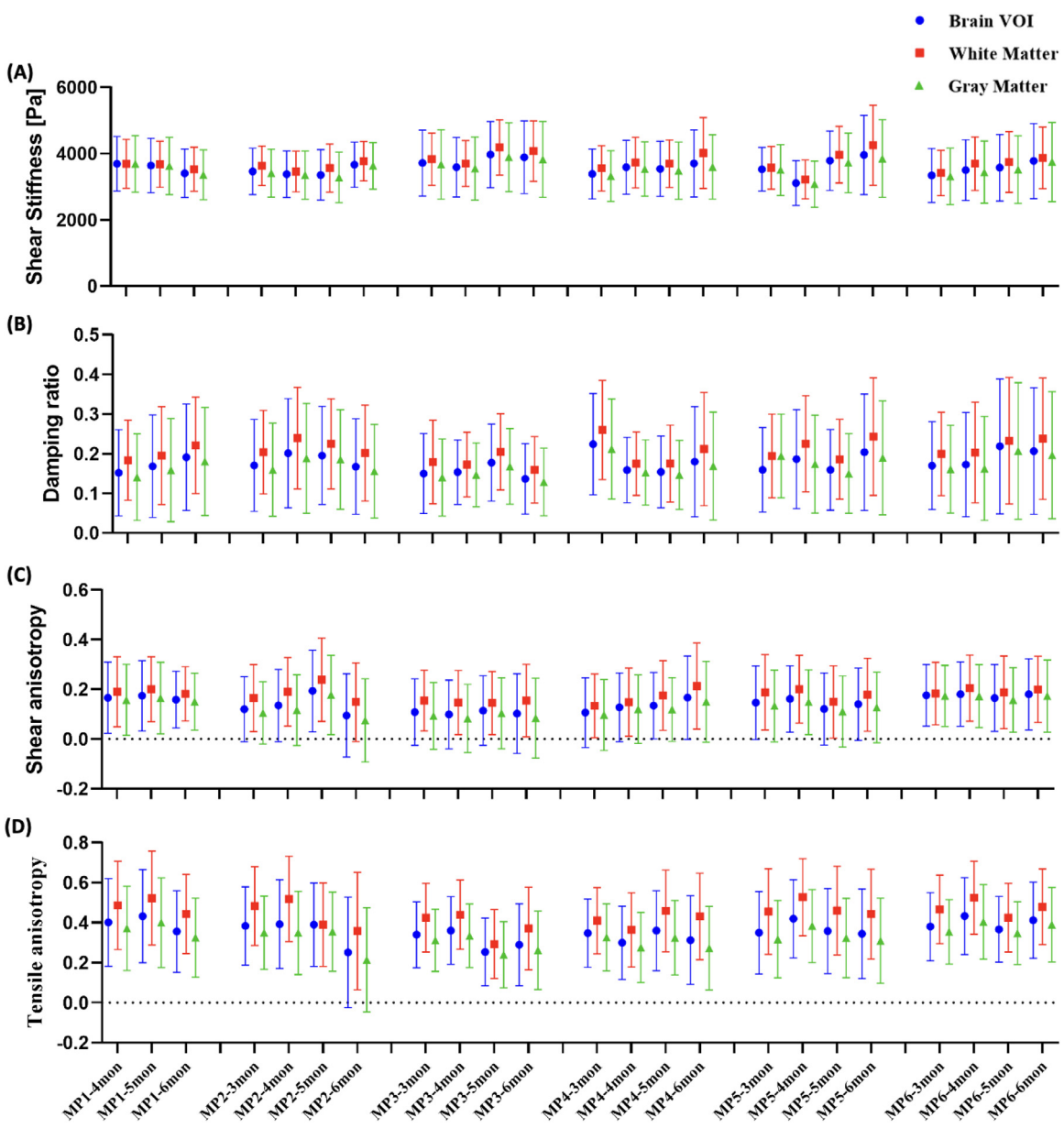

Fig. 8. Mean values of NLI-estimated mechanical properties for each animal, at each age, in the whole brain VOI, in white matter, and in gray matter. (A) Shear stiffness μ. (B) Damping ratio, ξ. (C) Shear anisotropy, ϕ. (D) Tensile anisotropy, ζ. Error bars denote ± 1 standard deviation.

a small central region. In a subset of scan dates, anisotropic (TI-NLI) and isotropic NLI were performed using only data from a single actuator configuration (Supplementary Figs. S5 and S6). While estimates of mechanical parameters using single data sets are similar to those obtained with data from multiple actuator configurations, using multiple fields appears to provide more consistent symmetry. Isotropic NLI generates higher stiffness estimates where TI-NLI finds higher anisotropy, suggesting again that the higher effective stiffness of WM may be due to its anisotropic properties.

Some local features of parameter fields correspond to anatomical features that are not captured well by the TI model. Notably, in Fig. 5, very high estimates of damping ratio ξ, were observed for all four input combinations in the center part of slice II, which contains the lateral ventricle. Model-data mismatch in fluid regions (which are modeled as a viscoelastic solid in TI-NLI) might account for these high ξ estimates as well as for the higher variance in this region (Fig. 7B). However, regions containing fluid (such as the ventricles) are small (<10% of brain volume) and largely eliminated by CSF masks applied to NLI results, reducing the effects of such artifacts. TI-NLI requires regularization to maintain stability, leading to incomplete contrast recovery near high property gradients, which can make it difficult to delineate small structures. This is particularly evident in minipig brain due to the much smaller size compared to humans.

Our estimates of shear stiffness, μ, are in the range of 3500 to 4000 Pa, and damping ratio, ξ, in the range of 0.1 to 0.3. The shear stiffness is somewhat higher than estimated in a previous study of minipig brain at 100 Hz using isotropic MRE and local direct inversion of the wave equation ($\mu \approx 2500$ Pa, $\xi \approx 0.2$) (Guertler et al., 2018). Differences in parameter estimates may be due to the different regions included in the two studies, as well as to differences between the inversion methods used. Accounting for effects of frequency, the current estimates of shear stiffness are consistent with estimates of μ from ~2600-2800 Pa (WM higher than GM) in human brain at 50 Hz using anisotropic MRE (Smith et al., 2022), and current estimates of damping are similar to estimates of ξ in human brain at 50 Hz using isotropic MRE (McIlvain et al., 2018). In WM, current estimates of shear anisotropy (ϕ) are in the range of 0.15-

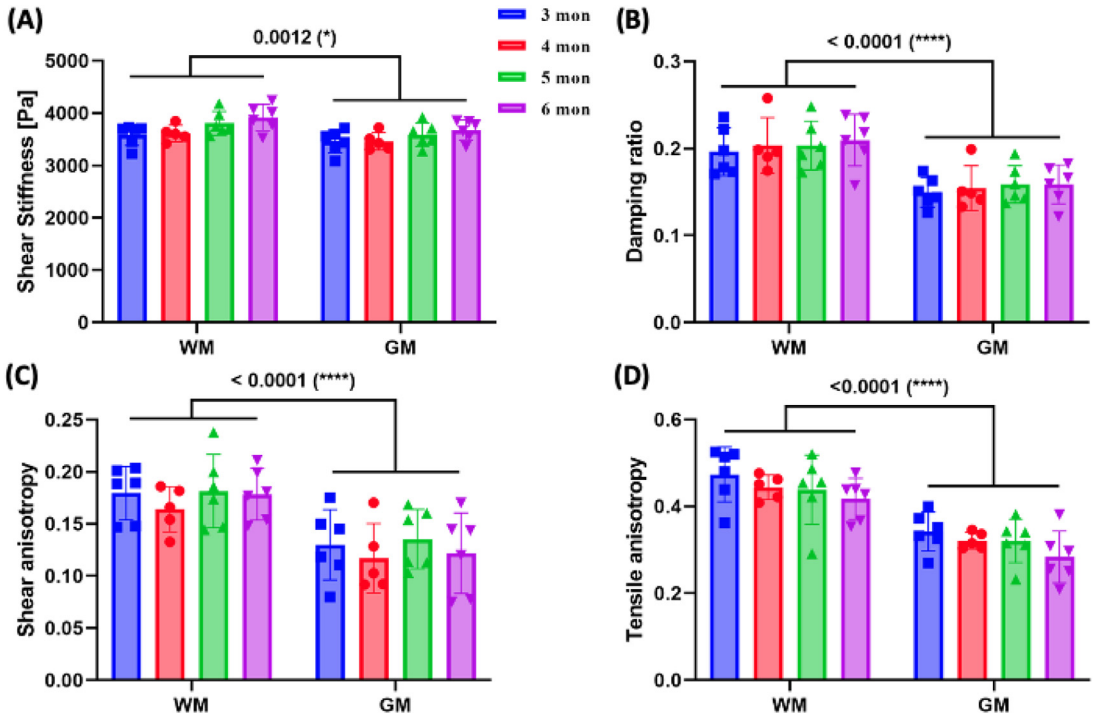

Fig. 9. Mean NLI-estimated mechanical properties of white matter and gray matter for all six minipigs. Each marker represents the mean value for an individual minipig at a specific age; error bars show standard deviations of these values. (A) Shear stiffness, μ. (B) Damping ratio, ξ. (C) Shear anisotropy, ϕ. (D) Tensile anisotropy, ζ.

0.25, and tensile anisotropy (ζ) are between 0.35-0.55, (Fig. 9), similar to estimates in human WM (Smith et al., 2020; Smith et al., 2022).

Some small negative values of ϕ and ζ are occasionally observed, especially in GM. Negative ϕ means that the material appears softer when sheared in planes parallel to the estimated dominant fiber direction than in planes perpendicular to the fiber axis. This could be plausible physically, depending on how the fibers interact with the surrounding matrix material. However, the most likely explanation is that the estimated "fiber axis" does not actually represent a dominant fiber direction, but simply the direction of maximal diffusivity, which is almost random in (nearly) isotropic GM. A prior simulation study (McGarry et al., 2021) showed that added noise in fiber direction does affect estimates, but the impact is relatively small: less than 10% decrease in anisotropy estimates occurred at high (50%) noise levels. Similarly, negative ζ means that the material appears softer when stretched in the direction of maximal diffusivity. This could happen in a truly fibrous material if fibers are softer than matrix, but is more likely if the direction of maximal diffusivity is not actually a dominant fiber direction. In GM, there is no clear association of "direction of maximal diffusivity" with any fiber axis. In materials where the true value of a parameter is zero, it is natural for estimates to vary, in both plus and minus directions. Therefore, in GM, which appears close to isotropic, small negative values of ϕ and ζ are to be expected.

We observed a small increase in shear stiffness, μ, with age in both WM and GM, consistent with prior studies of brain maturation in the mouse (Guo et al., 2019, Pong et al., 2016, Shulyakov et al., 2011), and the adolescent human brain (Ozkaya et al., 2021). No statistically significant changes in damping (ξ) or mechanical anisotropy (ϕ or ζ) with age were detected. The lack of effect of age on damping is consistent with prior studies in the human brain (Hiscox et al., 2018; McIlvain et al., 2018). Tensile anisotropy exhibits a slight tendency to decrease with age, particularly in WM, although this effect is not statistically significant ($p = 0.2072$ in WM). This trend might be related to myelination, intracellular cytoskeletal linkages and cell-matrix attachment (Weickenmeier et al., 2016). While myelination increases diffusion anisotropy (FA), its effects on mechanical anisotropy are not clear. We speculate that a larger density of oligodendrocytes might increase WM stiffness perpendicular to fiber direction more than its stiffness parallel to the fiber axis, thus decreasing tensile anisotropy.

We acknowledge several limitations of this study. First, the minipig brain is small (< 110 cm^3), so that even using state-of-the-art imaging sequences and technology, images are acquired at a lower resolution, relative to brain anatomical structure, than typical human scans. Additionally, only female minipigs were used in this study. Future studies should also include male minipigs to clarify the effect of gender in brain development. Another limitation of this study is that MRE was performed at only one frequency (100 Hz). Inversion methods currently under development will allow us to incorporate data from multiple frequencies and enable us to model frequency-dependent behavior in the anisotropic parameters. The current NITI material model is designed to capture behavior of a material with a single dominant fiber direction. Parameter estimates will be inaccurate or difficult to interpret in regions with crossing fibers, as in some regions of brain WM. Such regions were assumed to correspond to voxels with "planar" diffusion ellipsoids, which were excluded from both the GM and WM regions analyzed in the current paper. Recent and ongoing work is aimed at incorporating material models into NLI to describe tissue with two fiber families (Hou et al., 2021). Isotropic viscosity was assumed in the current study for simplicity; the accuracy of this assumption should be investigated in future studies. The minipig's fully gyrencephalic brain and compressed WM maturation period make it an attractive model of human brain development, although an intrinsic limitation of all animal models is the inability to directly translate research findings to humans. Future work is warranted to systematically explore changes in anisotropic mechanical properties during human brain development.

5. Conclusion

This study is the first to investigate anisotropic mechanical properties in a large animal model during brain development. MRE data were

collected from multiple shear wave fields in the minipig brain and combined with DTI-derived fiber directions to estimate anisotropic mechanical properties by a novel inverse-FEM inversion method: TI-NLI. WM in the minipig is more anisotropic than GM, both structurally and mechanically, as well as more dissipative. WM is stiffer than GM, even when deformed in the plane of isotropy normal to the fiber axis; this difference in stiffness is amplified significantly by anisotropy when deformed in other planes. Brain development in the minipig from 3-6 months is associated with increasing tissue stiffness and increasing diffusion anisotropy, but no clear changes in damping or mechanical anisotropy. Anisotropic mechanical properties of brain tissue are of fundamental biophysical significance, and future studies with anisotropic MRE may improve our understanding of normal brain structure and function during development, aging, injury, and disease.

Declaration of Competing Interest

The authors declare that they have no known competing financial interests or personal relationships that could have appeared to influence the work reported in this paper.

Credit authorship contribution statement

Shuaihu Wang: Conceptualization, Data curation, Formal analysis, Methodology, Writing – original draft. **Charlotte A. Guertler:** Conceptualization, Data curation, Formal analysis, Methodology, Writing – review & editing. **Ruth J. Okamoto:** Data curation, Formal analysis, Methodology, Writing – review & editing. **Curtis L. Johnson:** Methodology, Funding acquisition, Resources, Writing – review & editing. **Matthew D.J. McGarry:** Methodology, Resources, Software, Writing – review & editing. **Philip V. Bayly:** Methodology, Resources, Supervision, Validation, Funding acquisition, Writing – review & editing.

Data availability

Data will be made available on request.

Acknowledgment

This work was supported by National Institutes of Health (NIH) Grant R01EB027577 and Office of Naval Research (ONR) Grant N00014-22-1-2198.

Data and code availability statements

Numerical data will be made available by simple request. Raw image files will be made available by request which includes a formal project outline and an agreement of data sharing.

Supplementary materials

Supplementary material associated with this article can be found, in the online version, at doi:10.1016/j.neuroimage.2023.120234.

References

Anderson, A.T., Van Houten, E.E.W., McGarry, M.D.J., Paulsen, K.D., Holtrop, J.L., Sutton, B.P., Georgiadis, J.G., Johnson, C.L., 2016. Observation of direction-dependent mechanical properties in the human brain with multi-excitation MR elastography. J. Mech. Behav. Biomed. Mater. 59, 538–546. doi:10.1016/j.jmbbm.2016.03.005.

Ashtari, M., Cervellione, K.L., Hasan, K.M., Wu, J., McIlree, C., Kester, H., Ardekani, B.A., Roofeh, D., Szeszko, P.R., Kumra, S., 2007. White matter development during late adolescence in healthy males: a cross-sectional diffusion tensor imaging study. Neuroimage 35 (2), 501–510. doi:10.1016/j.neuroimage.2006.10.047.

Atlan, L.S., Margulies, S.S., 2019. Frequency-dependent changes in resting state electroencephalogram functional networks after traumatic brain injury in piglets. J. Neurotrauma 36 (17), 2558–2578. doi:10.1089/neu.2017.5574.

Atlan, L.S., Smith, C., Margulies, S.S., 2018. Improved prediction of direction-dependent, acute axonal injury in piglets. J. Neurosci. Res. 96 (4), 536–544. doi:10.1002/jnr.24108.

Badachhape, A.A., Okamoto, R.J., Durham, R.S., Efron, B.D., Nadell, S.J., Johnson, C.L., Bayly, P.V., 2017. The relationship of three-dimensional human skull motion to brain tissue deformation in magnetic resonance elastography studies. J. Biomech. Eng. 139, 51002. doi:10.1115/1.4036146.

Barnea-Goraly, N., Menon, V., Eckert, M., Tamm, L., Bammer, R., Karchemskiy, A., Dant, C.C., Reiss, A.L., 2005. White matter development during childhood and adolescence: a cross-sectional diffusion tensor imaging study. Cereb. Cortex 15 (12), 1848–1854. doi:10.1093/cercor/bhi062.

Basser, P.J., Pierpaoli, C., 1996. Microstructural and physiological features of tissues elucidated by quantitative-diffusion-tensor MRI. J. Magn. Reson. B 111 (3), 209–219. doi:10.1006/jmrb.1996.0086.

Boulet, T., Kelso, M.L., Othman, S.F., 2013. Long-term *in vivo* imaging of viscoelastic properties of the mouse brain after controlled cortical impact. J. Neurotrauma 30 (17), 1512–1520. doi:10.1089/neu.2012.2788.

Clayton, E.H., Genin, G.M., Bayly, P.V., 2012. Transmission, attenuation and reflection of shear waves in the human brain. J. R. Soc. Interface 9 (76), 2899–2910. doi:10.1098/rsif.2012.0325.

Fang, M., Li, J., Gong, X., Antonio, G., Lee, F., Kwong, W.H., Wai, S.M., Yew, D.T., 2005. Myelination of the pig's brain: a correlated MRI and histological study. Neurosignals 14 (3), 102–108. doi:10.1159/000086292.

Faria, A.V., Zhang, J., Oishi, K., Li, X., Jiang, H., Akhter, K., Hermoye, L., Lee, S.K., Hoon, A., Stashinko, E., Miller, M.I., van Zijl, P.C., Mori, S., 2010. Atlas-based analysis of neurodevelopment from infancy to adulthood using diffusion tensor imaging and applications for automated abnormality detection. Neuroimage 52 (2), 415–428. doi:10.1016/j.neuroimage.2010.04.238.

Feng, Y., Okamoto, R.J., Namani, R., Genin, G.M., Bayly, P.V., 2013. Measurements of mechanical anisotropy in brain tissue and implications for transversely isotropic material models of white matter. J. Mech. Behav. Biomed. Mater. 23, 117–132. doi:10.1016/j.jmbbm.2013.04.007.

Fil, J.E., Joung, S., Zimmerman, B.J., Sutton, B.P., Dilger, R.N., 2021. High-resolution magnetic resonance imaging-based atlases for the young and adolescent domesticated pig (Sus scrofa). J. Neurosci. Methods 354, 109107. doi:10.1016/j.jneumeth.2021.109107.

Fovargue, D., Kozerke, S., Sinkus, R., Nordsletten, D., 2018. Robust MR elastography stiffness quantification using a localized divergence free finite element reconstruction. Med. Image Anal. 44, 126–142. doi:10.1016/j.media.2017.12.005.

Garimella, H.T., Kraft, RH., 2017. Modeling the mechanics of axonal fiber tracts using the embedded finite element method. Int. J. Numer. Meth. Biomed. Engng. 33, e2823. doi:10.1007/s10237-019-01273-8.

Giordano, C., Zappalà, S., Kleiven, S., 2017. Anisotropic finite element models for brain injury prediction: the sensitivity of axonal strain to white matter tract inter-subject variability. Biomech. Model. Mechanobiol. 16 (4), 1269–1293. doi:10.1007/s10237-017-0887-5.

Green, M.A., Geng, G., Qin, E., Sinkus, R., Gandevia, S.C., Bilston, L.E., 2013. Measuring anisotropic muscle stiffness properties using elastography. NMR Biomed. 26 (11), 1387–1394. doi:10.1002/nbm.2964.

Guertler, C.A., Okamoto, R.J., Ireland, J.A., Pacia, C.P., Garbow, J.R., Chen, H., Bayly, P.V., 2020. Estimation of Anisotropic Material Properties of Soft Tissue by MRI of Ultrasound-Induced Shear Waves. J. Biomech. Eng. 142 (3), 0310011–03100117. doi:10.1115/1.4046127.

Guertler, C.A., Okamoto, R.J., Schmidt, J.L., Badachhape, A.A., Johnson, C.L., Bayly, P.V., 2018. Mechanical properties of porcine brain tissue *in vivo* and *ex vivo* estimated by MR elastography. J. Biomech. 69, 10–18. doi:10.1016/j.jbiomech.2018.01.016.

Guidetti, M., Royston, T.J., 2018. Analytical solution for converging elliptic shear wave in a bounded transverse isotropic viscoelastic material with nonhomogeneous outer boundary. J. Acoust. Soc. Am. 144 (4), 2312. doi:10.1121/1.5064372.

Guidetti, M., Zampini, M.A., Jiang, Y., Gambacorta, C., Smejkal, J.P., Crutison, J., Pan, Y., Klatt, D., Royston, T.J., 2021. Axially- and torsionally-polarized radially converging shear wave MRE in an anisotropic phantom made via embedded direct ink writing. J. Mech. Behav. Biomed. Mater. 119, 104483. doi:10.1016/j.jmbbm.2021.104483.

Guo, J., Bertalan, G., Meierhofer, D., Klein, C., Schreyer, S., Steiner, B., Wang, S., Vieira da Silva, R., Infante-Duarte, C., Koch, S., Boehm-Sturm, P., Braun, J., 2019. Sack I. Brain maturation is associated with increasing tissue stiffness and decreasing tissue fluidity. Acta Biomater. 99, 433–442. doi:10.1016/j.actbio.2019.08.036.

Guo, J., Hirsch, S., Scheel, M., Braun, J., Sack, I., 2015. Three-parameter shear wave inversion in MR elastography of incompressible transverse isotropic media: Application to *in vivo* lower leg muscles. Magn. Reson. Med. 75 (4), 1537–1545. doi:10.1002/mrm.25740.

Hiscox, L.V., Johnson, C.L., McGarry, M.D.J., Marshall, H., Ritchie, C.W., van Beek, E.J.R., Roberts, N., Starr, J.M., 2020. Mechanical property alterations across the cerebral cortex due to Alzheimer's disease. Brain Commun. 2 (1). doi:10.1093/braincomms/fcz049, fcz049.

Hiscox, L.V., Johnson, C.L., McGarry, M.D.J., Perrins, M., Littlejohn, A., van Beek, E.J.R., Roberts, N., Starr, J.M., 2018. High-resolution magnetic resonance elastography reveals differences in subcortical gray matter viscoelasticity between young and healthy older adults. Neurobiol. Aging 65, 158–167. doi:10.1016/j.neurobiolaging.2018.01.010.

Hiscox, L.V., Schwarb, H., McGarry, M.D.J., Johnson, C.L., 2021. Aging brain mechanics: Progress and promise of magnetic resonance elastography. Neuroimage 232, 117889. doi:10.1016/j.neuroimage.2021.117889.

Hou, Z., Bayly, P.V., Okamoto, RJ., 2021. Shear wave speeds in nearly-incompressible fibrous materials with two fiber families. J. Acoust. Soc. Am. 149 (2), 1097. doi:10.1121/10.0003528.

Hou, Z., Guertler, C.A., Okamoto, R.J., Chen, H., Garbow, J.R., Kamilov, U.S., Bayly, P.V., 2022. Estimation of the mechanical properties of a transversely isotropic material

from shear wave fields via artificial neural networks. J. Mech. Behav. Biomed. Mater. 126, 105046. doi:10.1016/j.jmbbm.2021.105046.
Irfanoglu, M.O., Modi, P., Nayak, A., Hutchinson, E.B., Sarlls, J., Pierpaoli, C., 2015. DR-BUDDI (diffeomorphic registration for blip-up blip-down diffusion imaging) method for correcting echo planar imaging distortions. Neuroimage 106, 284–299. doi:10.1016/j.neuroimage.2014.11.042.
Johnson, C.L., McGarry, M.D.J., Van Houten, E.E.W., Weaver, J.B., Paulsen, K.D., Sutton, B.P., Georgiadis, J.G., 2013. Magnetic resonance elastography of the brain using multishot spiral readouts with self-navigated motion correction. Magn. Reson. Med. 70, 404–412. doi:10.1002/mrm.24473.
Klatt, D., Hamhaber, U., Asbach, P., Braun, J., Sack, I., 2007. Noninvasive assessment of the rheological behavior of human organs using multifrequency MR elastography: a study of brain and liver viscoelasticity. Phys. Med. Biol. 52 (24), 7281–7294. doi:10.1088/0031-9155/52/24/006.
Mädler, B., Drabycz, S.A., Kolind, S.H., Whittall, K.P., MacKay, A.L., 2008. Is diffusion anisotropy an accurate monitor of myelination? Correlation of multicomponent T2 relaxation and diffusion tensor anisotropy in human brain. Magn. Reson. Imaging 26 (7), 874–888. doi:10.1016/j.mri.2008.01.047.
Manduca, A., Muthupillai, R., Rossman, P.J., Greenleaf, J.F., Ehman, R.L., 1996. Image Processing for Magnetic Resonance Elastography (Medical Imaging 1996). SPIE doi:10.1117/12.237965.
Manduca, A., Oliphant, T.E., Dresner, M.A., Mahowald, J.L., Kruse, S.A., Amromin, E., Felmlee, J.P., Greenleaf, J.F., Ehman, RL., 2001. Magnetic resonance elastography: non-invasive mapping of tissue elasticity. Med. Image Anal. 5 (4), 237–254. doi:10.1016/s1361-8415(00)00039-6.
Mariappan, Y.K., Glaser, K.J., Ehman, R.L., 2010. Magnetic resonance elastography: a review. Clin. Anat. 23 (5), 497–511. doi:10.1002/ca.21006.
Miller, R., Kolipaka, A., Nash, M.P., Young, A.A., 2018. Estimation of transversely isotropic material properties from magnetic resonance elastography using the optimised virtual fields method. Int. J. Numer. Method Biomed. Eng. 34 (6). doi:10.1002/cnm.2979, e2979.
McGarry, M., Houten, E.V., Guertler, C., Okamoto, R., Smith, D., Sowinski, D., Johnson, C., Bayly, P., Weaver, J., Paulsen, K., 2021. A heterogenous, time harmonic, nearly incompressible transverse isotropic finite element brain simulation platform for MR elastography. Phys. Med. Biol. 66 (5), 10. doi:10.1088/1361-6560/ab9a84.
McGarry, M., Van Houten, E., Sowinski, D., Jyoti, D., Smith, D.R., Caban-Rivera, D.A., McIlvain, G., Bayly, P., Johnson, C.L., Weaver, J., Paulsen, K., 2022. Mapping heterogenous anisotropic tissue mechanical properties with transverse isotropic nonlinear inversion MR elastography. Med. Image Anal. 78, 102432. doi:10.1016/j.media.2022.102432.
McGarry, M.D., Van Houten, E.E., Johnson, C.L., Georgiadis, J.G., Sutton, B.P., Weaver, J.B., Paulsen, K.D., 2012. Multiresolution MR elastography using nonlinear inversion. Med. Phys. 39 (10), 6388–6396. doi:10.1118/1.4754649.
McGarry, M.D., Van Houten, E.E., 2008. Use of a Rayleigh damping model in elastography. Med. Biol. Eng. Comput. 46 (8), 759–766. doi:10.1007/s11517-008-0356-5.
McGorry, P.D., Purcell, R., Goldstone, S., Amminger, G.P., 2011. Age of onset and timing of treatment for mental and substance use disorders: implications for preventive intervention strategies and models of care. Curr. Opin. Psychiatry 24 (4), 301–306. doi:10.1097/yco.0b013e3283477a09.
McIlvain, G., Cerjanic, A.M., Christodoulou, A.G., McGarry, M.D.J., Johnson, C.L., 2022. OSCILLATE: A low-rank approach for accelerated magnetic resonance elastography. Magn. Reson. Med. doi:10.1002/mrm.29308.
McIlvain, G., Schwarb, H., Cohen, N.J., Telzer, E.H., Johnson, C.L., 2018. Mechanical properties of the *in vivo* adolescent human brain. Dev. Cogn. Neurosci. 34, 27–33. doi:10.1016/j.dcn.2018.06.001.
Netzley, A.H., Hunt, R.D., Franco-Arellano, J., Arnold, N., Vazquez, A.I., Munoz, K.A., Colbath, A.C., Bush, T.R., Pelled, G., 2021. Multimodal characterization of Yucatan minipig behavior and physiology through maturation. Sci. Rep. 11, 22688. doi:10.1038/s41598-021-00782-w.
Okamoto, R.J., Clayton, E.H., Bayly, P.V., 2011. Viscoelastic properties of soft gels: comparison of magnetic resonance elastography and dynamic shear testing in the shear wave regime. Phys. Med. Biol. 56 (19), 6379–6400. doi:10.1088/0031-9155/56/19/014.
Oliphant, T.E., Manduca, A., Ehman, R.L., Greenleaf, J.F., 2001. Complex-valued stiffness reconstruction for magnetic resonance elastography by algebraic inversion of the differential equation. Magn. Reson. Med. 45 (2), 299–310. doi:10.1002/1522-2594(200102)45, 2%3C299::aid-mrm1039%3E3.0.co;2-o.
Opel, N., Goltermann, J., Hermesdorf, M., Berger, K., Baune, B.T., Dannlowski, U., 2020. Cross-disorder analysis of brain structural abnormalities in six major psychiatric disorders: a secondary analysis of mega- and meta-analytical findings from the enigma consortium. Biol. Psychiatry 88 (9), 678–686. doi:10.1016/j.biopsych.2020.04.027.
Ozkaya, E., Fabris, G., Macruz, F., Suar, Z.M., Abderezaei, J., Su, B., et al., 2021. Viscoelasticity of children and adolescent brains through MR elastography. J. Mech. Behav. Biomed. Mater. 115, 104229. doi:10.1016/j.jmbbm.2020.104229.
Pierpaoli, C., Walker, L., Irfanoglu, M.O., Barnett, A., Basser, P., Chang, L.C., Koay, C., Pajevic, S., Rohde, G., Sarlls, J., Wu, M., 2010. TORTOISE: an integrated software package for processing of diffusion MRI data. In: Proceedings of the ISMRM 18th Annual Meeting. Stockholm, Sweden. abstract #1597.
Pong, A.C., Jugé, L., Cheng, S., Bilston, L.E., 2016. Longitudinal measurements of postnatal rat brain mechanical properties *in-vivo*. J. Biomech. 49 (9), 1751–1756. doi:10.1016/j.jbiomech.2016.04.005.
Qiu, A., Mori, S., Miller, MI., 2015. Diffusion tensor imaging for understanding brain development in early life. Annu. Rev. Psychol. 66, 853–876. doi:10.1146/annurev-psych-010814-015340.
Romano, A., Guo, J., Prokscha, T., Meyer, T., Hirsch, S., Braun, J., Sack, I., Scheel, M., 2014. *In vivo* waveguide elastography: effects of neurodegeneration in patients with amyotrophic lateral sclerosis. Magn. Reson. Med. 72 (6), 1755–1761. doi:10.1002/mrm.25067.
Romano, A., Scheel, M., Hirsch, S., Braun, J., 2012. Sack I. *In vivo* waveguide elastography of white matter tracts in the human brain. Magn. Reson. Med. 68 (5), 1410–1422. doi:10.1002/mrm.24141.
Ryan, M.C., Sherman, P., Rowland, L.M., Wijtenburg, S.A., Acheson, A., Fieremans, E., Veraart, J., Novikov, D.S., Hong, L.E., Sladky, J., Peralta, P.D., Kochunov, P., McGuire, S.A., 2018. Miniature pig model of human adolescent brain white matter development. J. Neurosci. Methods 296, 99–108. doi:10.1016/j.jneumeth.2017.12.017.
Sack, I., Beierbach, B., Wuerfel, J., Klatt, D., Hamhaber, U., Papazoglou, S., Martus, P., Braun, J., 2009b. The impact of aging and gender on brain viscoelasticity. Neuroimage 46 (3), 652–657. doi:10.1016/j.neuroimage.2009.02.040.
Sack, I., Johrens, K., Wurfel, J., Braun, J., 2013. Structure-sensitive elastography: on the viscoelastic powerlaw behavior of *in vivo* human tissue in health and disease. Soft Matter 9, 5672–5680. doi:10.1039/C3SM50552A.
Sack, I., Rump, J., Elgeti, T., Samani, A., Braun, J., 2009a. MR elastography of the human heart: noninvasive assessment of myocardial elasticity changes by shear wave amplitude variations. Magn. Reson. Med. 61 (3), 668–677. doi:10.1002/mrm.21878.
Schmidt, J.L., Tweten, D.J., Badachhape, A.A., Reiter, A.J., Okamoto, R.J., Garbow, J.R., Bayly, P.V., 2018. Measurement of anisotropic mechanical properties in porcine brain white matter ex vivo using magnetic resonance elastography. J. Mech. Behav. Biomed. Mater. 79, 30–37. doi:10.1016/j.jmbbm.2017.11.045.
Schmidt, J.L., Tweten, D.J., Benegal, A.N., Walker, C.H., Portnoi, T.E., Okamoto, R.J., Garbow, J.R., Bayly, P.V., 2016. Magnetic resonance elastography of slow and fast shear waves illuminates differences in shear and tensile moduli in anisotropic tissue. J. Biomech. 49 (7), 1042–1049. doi:10.1016/j.jbiomech.2016.02.018.
Schomberg, D.T., Tellez, A., Meudt, J.J., Brady, D.A., Dillon, K.N., Arowolo, F.K., Wicks, J., Rousselle, S.D., Shanmuganayagam, D., 2016. Miniature swine for preclinical modeling of complexities of human disease for translational scientific discovery and accelerated development of therapies and medical devices. Toxicol. Pathol. 44 (3), 299–314. doi:10.1177/0192623315618292.
Shulyakov, A.V., Cenkowski, S.S., Buist, R.J., Del Bigio, M.R., 2011. Age-dependence of intracranial viscoelastic properties in living rats. J. Mech. Behav. Biomed. Mater. 4 (3), 484–497. doi:10.1016/j.jmbbm.2010.12.012.
Sinkus, R., Tanter, M., Catheline, S., Lorenzen, J., Kuhl, C., Sondermann, E., Fink, M., 2005. Imaging anisotropic and viscous properties of breast tissue by magnetic resonance-elastography. Magn. Reson. Med. 53 (2), 372–387. doi:10.1002/mrm.20355.
Smith, D.R., Caban-Rivera, D.A., McGarry, M.D., Williams, L.T., McIlvain, G., Okamoto, R.J., Van Houten, E.E., Bayly, P.V., Paulsen, K.D., Johnson, C.L., 2022. Anisotropic mechanical properties in the healthy human brain estimated with multi-excitation transversely isotropic MR elastography. Brain Multiphys. 3, 10005. doi:10.1016/j.brain.2022.100051.
Smith, D.R., Guertler, C.A., Okamoto, R.J., Romano, A.J., Bayly, P.V., Johnson, C.L., 2020. Multi-excitation magnetic resonance elastography of the brain: wave propagation in anisotropic white matter. J. Biomech. Eng. 142 (7), 0710051–0710059. doi:10.1115/1.4046199.
Smith, S.M., Jenkinson, M., Woolrich, M.W., Beckmann, C.F., Behrens, T., Johansen-Berg, H., Bannister, P.R., De Luca, M., Drobnjak, I., Flitney, D.E., Niazy, R.K., Saunders, J., Vickers, J., Zhang, Y., De, S.N., Brady, J.M., Matthews, P.M., 2004. Advances in functional and structural MR image analysis and implementation as FSL. Neuroimage 23, S208–S219. doi:10.1016/j.neuroimage.2004.07.051.
Swindle, M.M., Makin, A., Herron, A.J., Clubb Jr, F.J., Frazier, K.S., 2012. Swine as models in biomedical research and toxicology testing. Vet. Pathol. 49 (2), 344–356. doi:10.1177/0300985811402846.
Tweten, D.J., Okamoto, R.J., Bayly, P.V., 2018. Requirements for accurate estimation of anisotropic material parameters by magnetic resonance elastography: a computational study. Magn. Reson. Med. 78 (6), 2360–2372. doi:10.1002/mrm.26600.
Tweten, D.J., Okamoto, R.J., Schmidt, J.L., Garbow, J.R., Bayly, P.V., 2015. Estimation of material parameters from slow and fast shear waves in an incompressible, transversely isotropic material. J. Biomech. 48 (15), 4002–4009. doi:10.1016/j.jbiomech.2015.09.009.
Van Houten, E.E., Miga, M.I., Weaver, J.B., Kennedy, F.E., Paulsen, K.D., 2001. Three-dimensional subzone-based reconstruction algorithm for MR elastography. Magn. Reson. Med. 45 (5), 827–837. doi:10.1002/mrm.1111.
Weickenmeier, J., de Rooij, R., Budday, S., Steinmann, P., Ovaert, T.C., 2016. Kuhl E. Brain stiffness increases with myelin content. Acta Biomater. 42, 265–272. doi:10.1016/j.actbio.2016.07.040.
Westin, C.F., Maier, S.E., Mamata, H., Nabavi, A., Jolesz, F.A., Kikinis, R., 2002. Processing and visualization for diffusion tensor MRI. Med. Image Anal. 6 (2), 93–108. doi:10.1016/s1361-8415(02)00053-1.
Yushkevich, P.A., Piven, J., Hazlett, H.C., Smith, R.G., Ho, S., Gee, J.C., Gerig, G., 2006. User-guided 3D active contour segmentation of anatomical structures: significantly improved efficiency and reliability. Neuroimage 31 (3), 1116–1128. doi:10.1016/j.neuroimage.2006.01.015.
Zhang, J., Green, M.A., Sinkus, R., Bilston, L.E., 2011. Viscoelastic properties of human cerebellum using magnetic resonance elastography. J. Biomech. 44 (10), 1909–1913. doi:10.1016/j.jbiomech.2011.04.034.